

## Wideband MIMO Channel Capacity Analysis in Multiprobe Anechoic Chamber Setups

Fan, Wei; Kyosti, Pekka; Nielsen, Jesper Ødum; Pedersen, Gert F.

*Published in:*  
I E E E Transactions on Vehicular Technology

*DOI (link to publication from Publisher):*  
[10.1109/TVT.2015.2435813](https://doi.org/10.1109/TVT.2015.2435813)

*Publication date:*  
2016

*Document Version*  
Early version, also known as pre-print

[Link to publication from Aalborg University](#)

*Citation for published version (APA):*  
Fan, W., Kyosti, P., Nielsen, J. Ø., & Pedersen, G. F. (2016). Wideband MIMO Channel Capacity Analysis in Multiprobe Anechoic Chamber Setups. *I E E E Transactions on Vehicular Technology*, 65(5), 2861 - 2871.  
<https://doi.org/10.1109/TVT.2015.2435813>

### General rights

Copyright and moral rights for the publications made accessible in the public portal are retained by the authors and/or other copyright owners and it is a condition of accessing publications that users recognise and abide by the legal requirements associated with these rights.

- Users may download and print one copy of any publication from the public portal for the purpose of private study or research.
- You may not further distribute the material or use it for any profit-making activity or commercial gain
- You may freely distribute the URL identifying the publication in the public portal -

### Take down policy

If you believe that this document breaches copyright please contact us at [vbn@aub.aau.dk](mailto:vbn@aub.aau.dk) providing details, and we will remove access to the work immediately and investigate your claim.

# Wideband MIMO Channel Capacity Analysis in Multi-probe Anechoic Chamber Setups

Wei Fan, Pekka Kyösti, Jesper Ø. Nielsen, and Gert F. Pedersen

**Abstract**—This paper discusses over the air (OTA) testing for multiple input multiple output (MIMO) capable terminals with emphasis on wideband MIMO channel capacity analysis in a multi-probe anechoic chamber setup. In the literature, the spatial correlation simulation accuracy at the receiver (Rx) side has been used to determine the test area size for a limited number of probes. However, it is desirable that the test area size is defined in terms of data rate deviation of the simulated channel in the laboratory from that of the target channel model. This paper reports MIMO capacity analysis results for wideband spatio-temporal channel models, with emphasis on the impact of spatial correlation at the transmit (Tx) side, the channel model, and the spatial correlation at the Rx side on the capacity simulation accuracy. Simulation results show that the number of probes is irrelevant to capacity simulation accuracy when the spatial correlation at the Tx side is in the high region (e.g.  $\rho > 0.7$ ). Furthermore, when correlation at the Tx side is low, the spatial correlation accuracy is less critical with small correlation at the Rx side. The simulation results are further supported by measurements in a practical multi-probe anechoic chamber setup. The capacity simulation accuracy is shown to be a valid measure to determine the test area size.

**Index Terms**—MIMO OTA testing, multi-probe, anechoic chamber, wideband channel capacity, test area size

## I. INTRODUCTION

The capacity of wireless systems can be enhanced by the use of multiple antennas at both the transmitter (Tx) and the receiver (Rx) ends [1]. New wireless standards such as LTE and LTE advanced have adopted multiple antenna technology. Over the air (OTA) testing methods of multiple-input multiple-output (MIMO) capable terminals have been actively discussed in standardization recently [2]. Due to its capability to physically synthesize electromagnetic fields in a shielded laboratory, the multi-probe anechoic chamber method has attracted great research attention. With the multi-probe anechoic chamber method, the radio propagation environment is reproduced as it would be experienced by the device under test (DUT) in the intended environment, but in a repeatable and controllable manner.

One major challenge with the multi-probe method is to create a realistic multipath environment around the test device in the laboratory. The test area is a geometrical area inside which the DUT is located. Acceptable error levels are defined for the channel simulation to ensure that the target

propagation environment is reproduced accurately inside the test area. The test area size depends directly on the number of probes used for synthesizing the radio channel [3], [4]. Many measurements have been performed to verify how well the emulated channel models follow the target models in terms of channel parameters such as power delay profile, power Doppler spectrum, cross polarization ratio (XPR) and spatial correlation at the Rx side, see e.g., [5], [6]. In the literature, to appropriately assess how accurately the simulated power angle spectrum (PAS) approximates the target PAS, the difference between the simulated spatial correlation and the target spatial correlation  $|\rho - \hat{\rho}|$  is chosen and used as a measure to determine the test zone size [3], [4], [7]. However, there is a concern whether  $|\rho - \hat{\rho}|$  is the optimal figure of merit (FoM) to determine the test area size, as the ultimate goal is to investigate whether performance of MIMO capable terminals, e.g. data throughput, can be accurately evaluated in the laboratory. Intuitively,  $|\rho - \hat{\rho}|$  is more critical when  $|\rho|$  is high, as MIMO performance (e.g. MIMO capacity) is highly sensitive to correlation in the high correlation region ( $|\rho| > 0.5$ ), while  $|\rho - \hat{\rho}|$  is less critical with small  $|\rho|$ , as the performance reduction is negligible [8]. It is also assumed that the test area size is determined by the spatial correlation simulation accuracy at the Rx side and the correlation at the Tx side is irrelevant.

The MIMO channel capacity in a particular environment depends highly on its propagation characteristics [8]. The effect of fading correlation on MIMO channel capacity has been investigated based on existing spatio-temporal wideband propagation channel models and extensive measurements reported in the literature [9]. Since the channels simulated in the multi-probe setup are only approximations, it is necessary to investigate how the capacity of the simulated channels matches with that of the target channel models. The impact of antenna correlation on channel capacity is well investigated in the literature, see e.g. in [10]. Also, it was pointed out in [11] that throughput results of tested MIMO terminals will be generally low in the SCME Urban macro (Uma) channel models due to the high correlation at the Tx side. However, no prior work has been reported on the impact of Tx antenna correlation on the test area size in the multi-probe setup. This paper reports MIMO capacity analysis results for wideband spatio-temporal channel models in the multi-probe anechoic chamber setup for the first time in the literature, to the best of our knowledge. Unlike previous work limited to spatial correlation simulation accuracy at the Rx side, the impact of the Tx side antenna arrays and the propagation environments are considered as well in this study. The main contributions of the paper are:

Wei Fan, Jesper Ø. Nielsen, and Gert F. Pedersen are with the Antennas, Propagation and Radio Networking section at the Department of Electronic Systems, Faculty of Engineering and Science, Aalborg University, Denmark (email: {wfa, jni, gfp}@es.aau.dk).

Pekka Kyösti is with Anite Telecoms Oy, Oulu, Finland (email: {pekka.kyosti}@anite.com).

- The MIMO capacities of the simulated channels in the multi-probe anechoic chamber setup are investigated and compared with the capacities of the target channel models.
- The impact of spatial correlation at the Tx side and at the Rx side on MIMO channel capacity is shown for the two representative channel models that are used in the 3GPP LTE standard for MIMO OTA testing [2]. The models are the SCME Urban micro (Umi) Tap delay line (TDL) model (six Laplacian shaped clusters) and the SCME Urban macro (Uma) TDL model from [12].
- The test zone size determined by MIMO capacity accuracy is discussed for the two representative wideband channel models.
- Measurement results in a practical multi-probe anechoic chamber setup further support the capacity analysis results.

## II. CAPACITY EVALUATION FOR MULTI-PROBE ANECHOIC CHAMBER SETUPS

### A. Channel Models

1) *Target channel model*: The target channel models adopted in this study are geometry-based stochastic channel models. The widely adopted MIMO channel models like SCME, WINNER, and IMT-Advanced models belong to this family [12]–[14]. Geometry-based modelling enables separation of channel propagation and antennas at the Rx and the Tx side [3]. A geometry-based channel model is composed of multiple clusters, each of which is modelled by the cluster power, delay, nominal angle of arrival (AoA), nominal angle of departure (AoD), angle spread of arrival (ASA), angle spread of departure (ASD), and cluster cross-polarization power ratio (XPR).

For  $N_t$  Tx antennas and  $N_r$  Rx antennas, the MIMO channel  $\mathbf{H} \in \mathbb{C}^{N_r \times N_t \times N_{ir} \times N_{taps}}$  can be represented by:

$$H(t, \tau) = \begin{bmatrix} h_{1,1}(t, \tau) & \cdots & h_{1,N_t}(t, \tau) \\ \vdots & \ddots & \vdots \\ h_{N_r,1}(t, \tau) & \cdots & h_{N_r,N_t}(t, \tau) \end{bmatrix}, \quad (1)$$

where  $\{h_{n_r, n_t}(t, \tau)\} \in \mathbb{C}^{N_{ir} \times N_{taps}}$  represents the time-variant channel impulse responses (CIRs) between the input of the  $n_t$ -th Tx antenna and output of the  $n_r$ -th Rx antenna with  $t = 1, \dots, N_{ir}$  and  $\tau = 1, \dots, N_{taps}$ .  $N_{ir}$  and  $N_{tap}$  are the number of time samples and maximum number of delays (resolvable paths), respectively. Note that each CIR contains the cascaded effect of a Tx antenna, the propagation environment and a Rx antenna. In this study, two representative channel models are selected as the target channel models: a) the SCME Umi TDL and b) the SCME Uma TDL.

Similar to [3], [7], an omnidirectional antenna pattern is assumed for each antenna element at the Rx side. The MIMO channel in the frequency domain  $\mathbf{H}_F = \{h_F(n_r, n_t, t, n_f)\} \in \mathbb{C}^{N_r \times N_t \times N_{ir} \times N_f}$  is obtained by performing the Fourier transform of  $\{h_{n_r, n_t}(t, \tau)\}$  in the delay domain, where  $N_f$  is the number of sub-carriers.  $N_f$  has to be large enough to ensure that each sub-channel experiences flat fading, i.e. sub-channel bandwidth is much smaller than channel coherence bandwidth.

### 2) *Simulated Channel Models in the Multi-probe Setup*:

The channel simulation method in multi-probe anechoic chamber setups, named as the prefaded signal synthesis (PFS) method, is detailed in [3]. The basic idea of the PFS technique is to transmit fading signals separately from the multiple probes. Different clusters are modeled independently. Each cluster is mapped to the probes based on the cluster PAS and probe angular locations. Each probe associated with the cluster transmits weighted independent fading sequences with identical statistics.

The target channel models adopted in MIMO OTA studies, i.e. geometry-based stochastic channel models, are generally dual-polarized. The PFS technique is capable of generating dual polarized channel as well. The basic idea is that the vertical and horizontal polarizations are treated independently and separately. That is, a set of power weights are allocated to the vertically polarized probes to reproduce the spatial characteristics in the vertical polarization, while another set of power weights for the horizontally polarized probes is used to reproduce the target channel spatial characteristics of the target channel in the horizontal polarization. If the same impinging power angular spectrum is assumed for both polarizations, then the same set of weights are utilized. The XPR is the ratio of average power between the vertical polarization and horizontal polarization, respectively. The XPR of the simulated channels is achieved by controlling the ratio of the total power allocated to the vertically polarized probes and horizontally polarized probes. With the PFS technique, the instantaneous fading field in the test area, however, will always be elliptically polarized for each time instant. With the field synthesis technique, e.g. the plane wave synthesis technique [3], it is possible to control the polarization of the field (e.g. linear, circular, or elliptical polarization). However, both phase and amplitude calibration of the probes are required. For the sake of simplicity, the target channel models are limited to a single polarization in the discussion in the paper, although the capacity analysis proposed in the paper is applicable to dual-polarized channels as well.

A virtual array consisting of omnidirectional Rx antenna elements is assumed in the paper. This assumption is generally adopted in multi-probe anechoic chamber studies. The basic idea is that, the Rx antennas are considered inherently during testing, and the focus is generally on the channel simulation part. That is, the channel simulation and the Rx antennas are considered separately. A similar concept is adopted in the geometry based channel models, where the antennas at the Tx/Rx side and the propagation channel are modeled separately. Omnidirectional antenna patterns are used, as the DUT antenna pattern is typically not known beforehand. Furthermore, if some antenna patterns are embedded in the channel model, the OTA performance will depend on both the antenna pattern embedded in the channel as well as the antenna pattern in the DUT, which is obviously undesirable. The impact of realistic Rx radiation pattern, which includes the Rx antenna coupling effect, on the channel simulation accuracy (mainly the antenna correlation accuracy) is investigated in [15]. Results show that the Rx antenna patterns have an impact on channel simulation accuracy and the channel simulation accuracy is

Table I  
TARGET CHANNEL MODEL FOR IDEA ILLUSTRATION

Cluster index	Power [dB]	Delay [ns]	AoA	AS
1	0	0	0°	35°
2	-3	1000	45°	35°

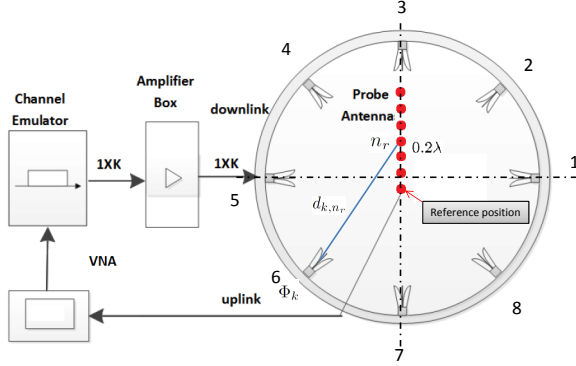


Figure 1. An illustration of the multi-probe setup.  $K = 8$  OTA probes are uniformly located on the OTA ring. A uniform linear array (ULA) consisting of 7 antenna elements with  $0.2\lambda$  as the Rx.

good if a sufficient number of probes is used, regardless of the Rx antenna patterns. For the capacity accuracy analysis, the Rx antenna pattern might impact the total received power level. That is, omnidirectional antennas would capture all the transmitted power from the probes in the chamber, while for realistic Rx antennas, there might be a difference in the receiver power due to the directive radiation patterns of the Rx antennas, which may impact the capacity and throughput results. This effect will be investigated in future work.

A simple channel model that consists of two clusters is selected as an example to demonstrate the idea of the PFS technique, as described in Table I. Eight uniformly located probes on an OTA ring are utilized to synthesize the target channel models, as illustrated in Figure 1. The weighted CIRs (originating from a single Tx antenna) that are transmitted from all the eight probes are shown in Figure 2. Each cluster is mapped to several OTA probes. Probe 1 (with angular location 0°) is dominant in synthesizing cluster 1, while probe 5 (with angular location 180°) does not contribute to cluster 1. This is expected, as the AoA of cluster 1 is 0°. Similar observations can be made for cluster 2. Optimization techniques to obtain power weights  $\omega = \{\omega_k\} \in \mathbb{R}^{K \times 1}$  have been discussed in [3], [16] and results from [16] are used here.

As detailed in [3], the CIRs from  $N_t$  Tx antennas to the  $k$ -th probe over time are  $\{h_k^{ota}(n_t, t, \tau)\} \in \mathbb{C}^{N_t \times N_{ir} \times N_{taps}}$  with  $k \in [1, K]$  and  $K$  is the total number of probes. The CIRs from the  $n_t$ -th Tx antenna to the  $n_r$ -th Rx antenna over time are  $\{\hat{h}_{n_r}(n_t, t, \tau)\} \in \mathbb{C}^{N_t \times N_{ir} \times N_{taps}}$  with:

$$\hat{h}_{n_r}(n_t, t, \tau) = \sum_{k=1}^K G_{n_r}(\Phi_k) \cdot h_k^{ota}(n_t, t, \tau) \cdot \alpha_{k,n_r} \quad (2)$$

where  $\Phi_k$  denotes the angular location for the  $k$ -th probe.  $G_{n_r}$  is the complex radiation pattern of the  $n_r$ -th Rx antenna, in

this case equal to 1 for  $n_r \in [1, N_r]$ , as an omnidirectional antenna pattern is assumed for all the Rx antennas.  $\alpha_{k,n_r}$  is the transfer coefficient from the  $k$ -th OTA probe to the  $n_r$ -th Rx antenna:

$$\alpha_{k,n_r} = L(d_{k,n_r}) \cdot \exp(-j \frac{2\pi}{\lambda} d_{k,n_r}), \quad (3)$$

where  $L(\cdot)$  is the pathloss term and  $d_{k,n_r}$  is the distance from the  $k$ -th OTA probe to the  $n_r$ -th Rx antenna element. The probe radiation pattern is assumed constant, as the test zone is much smaller than the OTA ring size in the study. For example, a test area of circle with diameter 16cm in a 2m radius OTA ring corresponds to around 5° probe angular width, which is much smaller than the half-power beam width (HPBW) of the probe antennas used in the multi-probe setup. The variation of the radiation patterns of the probes over the small angles, which corresponds to the test area, can hence be ignored. We denote the simulated channel in multi-probe setups as  $\hat{\mathbf{H}} = \{\hat{h}_{n_r}(n_t, t, \tau)\} \in \mathbb{C}^{N_r \times N_t \times N_{ir} \times N_{taps}}$ . Similarly we can obtain the simulated channel for multi-probe setups in the frequency domain  $\hat{\mathbf{H}}_F \in \mathbb{C}^{N_r \times N_t \times N_{ir} \times N_f}$ .

## B. Capacity Evaluation and Spatial Correlation

### 1) Capacity Evaluation:

a) *Target channel capacity:* In this paper, we assume that the channel knowledge is not available at the Tx side, and hence MIMO capacity is evaluated by assuming equal power allocation among the Tx antennas. The MIMO channel matrices are normalized in two ways in the literature [17]. One way is to ensure constant Tx power over the whole simulation period. Another way is to ensure constant instantaneous SNR, which corresponds to perfect power control at the Tx side. Note that similar conclusions can be drawn for the two normalizations, and the first normalization is used for the results presented in this work.  $\eta$  is the mean channel energy over time, Tx-Rx channels, and frequency. By normalizing by  $\eta$ , the mean received signal power is 1. We have,

$$\eta = \frac{1}{N_r N_t N_{ir} N_f} \sum_{n_r=1}^{N_r} \sum_{n_t=1}^{N_t} \sum_{i=1}^{N_{ir}} \sum_{f=1}^{N_f} |h_F(n_r, n_t, i, n_f)|^2 \quad (4)$$

The instantaneous channel capacity of the target channel model can be computed as [9]:

$$C(t) = \frac{1}{N_f} \sum_{n_f=1}^{N_f} \log_2 \det(\mathbf{I} + \frac{\sigma}{N_t \cdot \eta} \cdot H_F(t, n_f) \cdot H_F(t, n_f)^H), \quad (5)$$

where  $\mathbf{I}$  is the identity matrix, and  $H_F(t, n_f) \in \mathbb{C}^{N_r \times N_t}$  is the channel matrix of the  $n_f$ -th sub-carrier at time instant  $t$ .  $\sigma$  is the received SNR.  $(\cdot)^H$  denotes the Hermitian transpose. An average SNR of 15dB is assumed in the simulations and measurements unless otherwise stated.

Similar to the analysis performed in [9], we can obtain two kinds of statistics for the instantaneous capacity: a) capacity in the narrowband case (with  $N_f = 1$ ) and b) capacity in the wideband case with a sufficiently large  $N_f$  using Eq. (5). In [9], it was concluded that the wideband capacity results present similar mean and smaller variance as a result of averaging compared with the narrowband capacity.

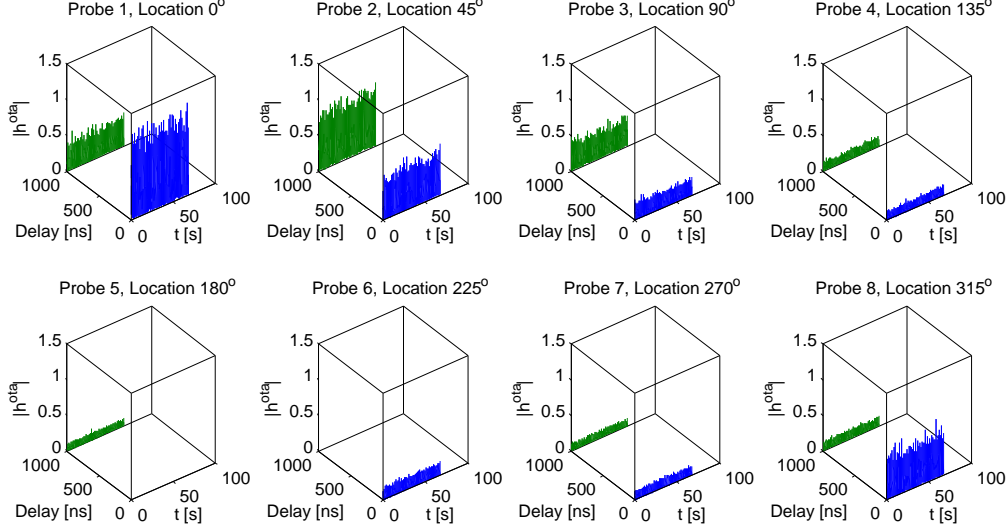


Figure 2. An illustration of CIRs for the target channel model detailed in Table I. Eight probes are used. Plots in blue corresponds to the CIRs associated with cluster 1 and plots in green denote the CIRs associated with cluster 2.

*b) Simulated channel capacity in the multi-probe setup:*

The channel normalization factor for the simulated channel model  $\hat{\eta}$  is defined similarly as in Eq (4), with  $\mathbf{H}_F$  replaced by  $\hat{\mathbf{H}}_F$ . Similarly, the instantaneous channel capacity of the simulated channel model  $\hat{C}(t)$  is calculated similarly as in Eq (5), with  $\mathbf{H}_F$  replaced by  $\hat{\mathbf{H}}_F$ .

*2) Spatial Correlation :*

*a) Target spatial correlation:* The correlation coefficient at the Tx and Rx can be obtained from wideband MIMO channel matrices detailed in Section II-A. The spatial correlation  $\rho_{ij}^{Tx}$  between a pair of channels from the  $i$ -th and the  $j$ -th Tx antennas, both arriving to the  $n_r$ -th Rx antenna is:

$$\begin{aligned} \rho_{ij}^{Tx} &= \text{corr} \left[ \sum_{\tau=1}^{N_{tap}} \mathbf{h}_{n_r,i}(\tau), \sum_{\tau=1}^{N_{tap}} \mathbf{h}_{n_r,j}(\tau) \right] \\ &= \frac{\sum_{t=1}^{N_{ir}} \left[ \sum_{\tau=1}^{N_{tap}} h_{n_r,i}(t, \tau) \cdot \sum_{\tau=1}^{N_{tap}} h_{n_r,j}^*(t, \tau) \right]}{\sqrt{\sum_{t=1}^{N_{ir}} \left| \sum_{\tau=1}^{N_{tap}} h_{n_r,i}(t, \tau) \right|^2 \cdot \sum_{t=1}^{N_{ir}} \left| \sum_{\tau=1}^{N_{tap}} h_{n_r,j}(t, \tau) \right|^2}} \end{aligned} \quad (6)$$

where  $\text{corr}()$  is the correlation operator.  $\mathbf{h}_{n_r,n_t}(\tau) = \{h_{n_r,n_t}(t, \tau)\} \in C^{N_{ir} \times 1}$  denotes the CIRs associated with delay  $\tau$  between the  $n_r$ -th Rx antenna and the  $n_t$ -th Tx antenna. In Eq. (6), the spatial correlation of the composite of all clusters is calculated. Cluster-wise spatial correlation can be calculated as well.

Similarly, the coefficient  $\rho_{ij}^{Rx}$ , denoting the correlation for channels between the  $i$ -th and the  $j$ -th Rx antenna, both from the same  $n_t$ -th Tx antenna, is

$$\rho_{ij}^{Rx} = \text{corr} \left[ \sum_{\tau=1}^{N_{tap}} \mathbf{h}_{i,n_t}(\tau), \sum_{\tau=1}^{N_{tap}} \mathbf{h}_{j,n_t}(\tau) \right] \quad (7)$$

Alternatively, the spatial correlation at the Tx and Rx side can be computed analytically, as detailed in [18]:

$$\rho_{ij} = \frac{\int_{-\pi}^{\pi} G_i(\phi) G_j^*(\phi) p(\phi) d\phi}{\sqrt{\int_{-\pi}^{\pi} p(\phi) |G_i(\phi)|^2 d\phi} \sqrt{\int_{-\pi}^{\pi} p(\phi) |G_j(\phi)|^2 d\phi}}, \quad (8)$$

where  $G_i$  and  $G_j$  are the complex radiation patterns of antenna element  $i$  and  $j$ , respectively, with a common phase center. Note that  $p(\phi)$  is the composite PAS which satisfies  $\int_{-\pi}^{\pi} p(\phi) d\phi = 1$ , with the composite PAS being the weighted sum of the cluster PAS with the weights equal to the path powers [13]. Cluster-wise spatial correlation can be calculated according to Eq. (8) as well, where  $p(\phi)$  denotes the cluster PAS. Eq. (8) can be used to calculate the spatial correlation based on the antenna configuration, antenna pattern and PAS defined both at the Tx and the Rx side.

*b) Simulated spatial correlation:* In the multi-probe anechoic chamber setup, the simulated spatial correlation at the Tx side  $\hat{\rho}^{Tx}$  and the Rx side  $\hat{\rho}^{Rx}$  can be calculated directly based on Eq. (6) and Eq. (7), with  $\mathbf{H}$  replaced by  $\hat{\mathbf{H}}$ . From Eq. (8), the simulated spatial correlation at the Tx side  $\hat{\rho}^{Tx}$  can be directly calculated as well, since the same continuous PAS as the target channel model is used for simulation at the Tx side [3]. However, at the Rx side, what the DUT sees is essentially a discrete PAS, characterized by the angular locations and power weights of the active probes. The simulated spatial correlation between the  $i$ -th and  $j$ -th element at the Rx side is:

$$\hat{\rho}_{ij}^{Rx} = \frac{\sum_k G_i(\Phi_k) \cdot G_j^*(\Phi_k) \cdot w_k}{\sqrt{\sum_k |G_i(\Phi_k)|^2 w_k} \cdot \sqrt{\sum_k |G_j(\Phi_k)|^2 w_k}} \quad (9)$$

where  $w_k$  is the power weight for the  $k$ -th probe.

The simulated spatial correlation at the Tx  $\hat{\rho}^{Tx}$  will always match the target  $\rho_{ij}^{Tx}$ , as the same continuous PAS is used. However, due to the limitation in the number of probes, a deviation between the simulated spatial correlation and the target spatial correlation at the Rx side exists, as discussed in [3], [7].

Note that the correlation at the Tx side is assumed independent from the considered Rx antenna. Similarly, correlation at the Rx side are assumed independent from the considered

Table II  
THREE SIMULATION SCENARIOS FOR CAPACITY ANALYSIS

	Tx configuration	Channel model	Rx configuration
A	2 co-located elements with X configuration, as detailed in [2]	Umi/Uma model	A 2 antenna element ULA with $0.5\lambda$ spacing
B	A 2 antenna element ULA with $10\lambda$ spacing	Umi/Uma model	A 2 antenna element ULA with $0.5\lambda$ spacing
C	A 4 antenna element ULA with $10\lambda$ spacing	Umi/Uma model	A 4 antenna element ULA with $0.5\lambda$ spacing

Tx antenna. This assumption is valid if the spatial stationarity regions are larger than the array sizes at the Tx and the Rx side, as explained in [19]. Note that it is assumed that the spatial stationarity region, where the propagation parameters (e.g. AoA and power angular spectrum) remain unchanged, is larger than the considered Tx and Rx array size for the geometry based stochastic channel models. In our study, the array dimensions at the Tx and the Rx are not unreasonably large and hence the assumption is valid in our investigation.

### III. SIMULATION RESULTS

#### A. Simulation Scenarios

To understand the impact of the Tx antenna array, the propagation environment and the Rx antenna array on the MIMO capacity and the simulated capacity accuracy, three scenarios are selected for the capacity analysis, as detailed in Table II. For all the three scenarios, antenna elements on the Tx side are ideal dipoles without considering the mutual coupling effect between them. Note that any antenna element and any array configuration can be used for simulation in the Tx configuration. The ULA broadsight direction is  $0^\circ$  for all the three scenarios in the Rx configuration. The ULAs consisting of vertical polarized ideal dipoles are considered. In scenario A, two  $\pm 45^\circ$  cross polarized dipoles are used at the Tx side. Similar setups are adopted in standardization for MIMO OTA testing [2]. In [2], channel models with XPR = 9dB are used, while only vertically polarized channel models are considered in this study for the sake of simplicity. In scenario C, a  $4 \times 4$  MIMO system is evaluated, with antenna spacing  $0.5\lambda$ , i.e., a maximal separation of  $1.5\lambda$  among antenna elements at the Rx side. The probe setup used in the simulation is illustrated in Figure 1. Note that the two SCME channel models are selected, as they have been standardized and adopted in MIMO OTA standards as well [2], [13]. Hence, the results shown in this paper apply directly to those standards.

#### B. Spatial Correlation

1) *Spatial correlation at the Rx side:* Spatial correlation results at the Rx side for the Umi and the Uma channel models for scenario C are shown in Figure 3 and Figure 4, respectively. Note that the spatial correlations are between two individual elements in the four-element array without accounting for correlation of the inner antennas (i.e.  $\rho_{11}^{Rx}$ ,  $\rho_{12}^{Rx}$ ,  $\rho_{13}^{Rx}$ ,  $\rho_{14}^{Rx}$ ).

Spatial correlation at Rx side for the SCME Umi TDL model

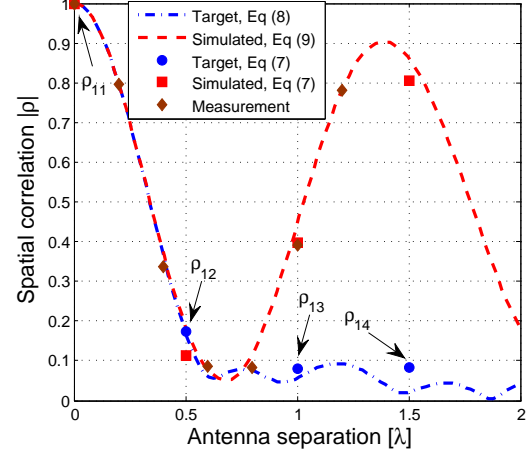


Figure 3. Spatial correlation at the Rx side for the SCME Umi TDL model for scenario C.  $\rho_{ij}$  in the figure denotes the correlation between two Rx antenna elements  $i$  and  $j$  for the Umi model.

Spatial correlation results at the Rx side for scenario A and B can be obtained from scenario C directly. The spatial correlation between the two Rx antennas in scenario B is the same as the spatial correlation between two neighboring Rx antennas in scenario C, since the same antenna element and antenna separation are used in the simulation for the two scenarios. The derivation of results for scenario A and B from scenario C is valid, as ideal dipoles without considering antenna coupling are assumed for all the scenarios. As we can see, the spatial correlation depends highly on the channel models. The spatial correlations calculated from Eq. (7) match well with the analytical formula results detailed in Section II-B both for the target and simulated spatial correlation. Generally, the simulated spatial correlation at the Rx side  $\hat{\rho}^{Rx}$  match well with the target  $\rho^{Rx}$ , when the Rx maximum antenna separation is smaller than  $0.7\lambda$ . When the antenna separation exceeds  $0.7\lambda$ , the simulated spatial correlation will be larger than the target for both channel models, as a result of the limited number of probes. Note that the spatial correlation results at the Rx side have been reported in the literature, see, e.g. [2], [6], [16], and is included here to explain the capacity results in the following sections. The measurement validation results presented in Figure 3, 4 and 5 are explained later in Section IV.

2) *Spatial correlation at the Tx side:* As the channel models are vertically polarized, the spatial correlation between two co-located (i.e. with antenna separation  $0\lambda$ ) dipoles at the Tx side for scenario A will be 1 for both channel models. Spatial correlation results at the Tx side for the Umi and Uma channel models in scenario C are shown in Figure 5. The spatial correlations at the Tx side are between two individual elements in the four-element array without accounting for correlation of the inner antennas (i.e.  $\rho_{11}^{Tx}$ ,  $\rho_{12}^{Tx}$ ,  $\rho_{13}^{Tx}$ ,  $\rho_{14}^{Tx}$ ). As expected, the simulated spatial correlation results match very



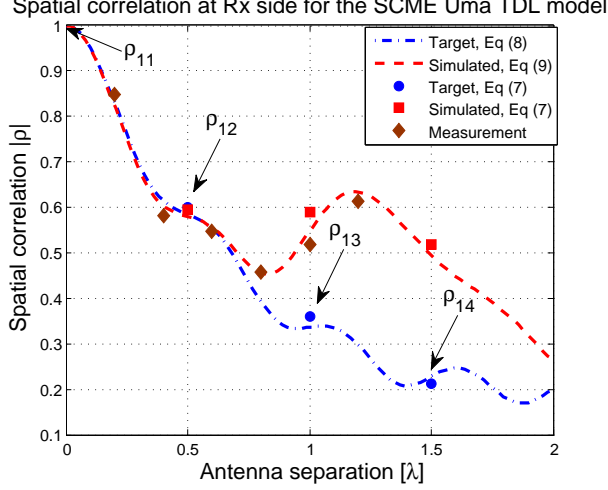


Figure 4. Spatial correlation at the Rx side for the SCME Uma TDL model for scenario C.  $\rho_{ij}$  in the figure denotes the correlation between two Rx antenna elements  $i$  and  $j$  for the Uma model.

well with the target correlation, independent of the antenna separation. The Tx antennas are de-correlated for the UMi channel model, with correlation dramatically falling to 0 at antenna separation  $10\lambda$ . However, for the Uma channel model, the Tx antennas are highly correlated, with  $\rho_{14}^{Tx} > 0.6$  for an antenna separation of  $30\lambda$ . Spatial correlation results at the Tx side for scenario B can be obtained from scenario C directly as well. The correlation at the Tx side, as shown in Eq. (8), depends both on the antenna array configuration at the Tx side and the channel spatial profile at the Tx side. For scenario B and C, the high Tx correlation observed for the Uma channel model is due to the fact that the AoDs of the dominant clusters are concentrated around the Tx array boresight direction [20]. The two channel models, i.e. the Umi channel model with low Tx correlation and the Uma channel model with high Tx correlation, are considered in the paper to demonstrate the impact of Tx correlation on test zone size. The Tx antennas in real sites are generally not highly correlated. But, high Tx correlation might be present in some scenarios, as shown in the measurement results in [21].

### C. Capacity Analysis

1) *Eigenvalue analysis*: The cumulative distribution functions (CDFs) of the ordered singular values are shown for scenario A (left) and B (right) in Figure 6. For scenario A, only one dominant singular value is present due to the high Tx correlation ( $|\rho^{Tx}| = 1$ ) for both channel models, and hence spatial multiplexing is not supported. For scenario B, two dominant singular values are present for both channel models. However, the Uma channel model is worse-conditioned due to the high Tx correlation. The CDF of the simulated channel models match well with the target channel models for scenario A and scenario B, as expected.

The CDFs of the ordered singular values are shown for scenario C in Figure 7. For the Uma channel models, the CDF

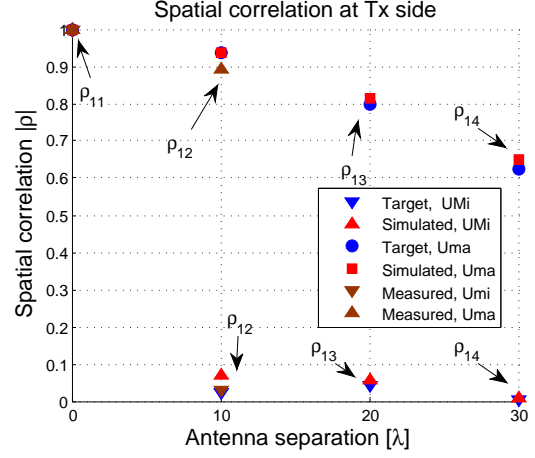


Figure 5. Spatial correlation at the Tx side for the SCME Umi TDL model and SCME Uma TDL model for scenario C.  $\rho_{ij}$  in the figure denotes the correlation between two Tx antenna elements  $i$  and  $j$  for the Umi model.

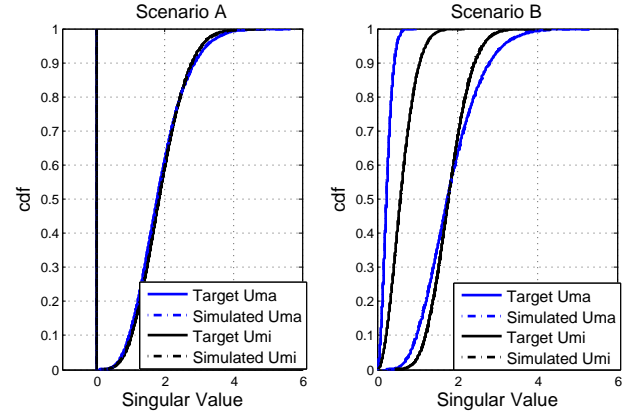


Figure 6. CDFs of the singular values for scenario A (left) and scenario B (right). Note that the plots for the simulated channels are on top of the plots for target channel models.

of the most dominant singular value is much larger than the other three singular values. The CDFs of the simulated channel match well with the target for the Uma channel model due to the high Tx correlation. As for the Umi channel model, deviations between the CDFs of the simulated channel and target channel exists, as a result of limited number of probes.

2) *Capacity in narrowband and wideband case*: Capacity results in the narrowband case (with  $N_f = 1$ ) and in the wideband case (with  $N_f = 201$  and bandwidth 20MHz in the simulations) are compared for all the scenarios. The difference between the mean of the wideband capacity and the mean of the narrowband capacity is negligible for all cases. The capacity variance is smaller in the wideband case compared with the narrowband case for all the scenarios, as a result of averaging. Figure 8 shows the instantaneous capacity in narrowband and wideband cases for the simulated Umi channel models for scenario C, where the mean capacity difference is less than 0.1 bits/s/Hz. The standard deviation of the wideband instantaneous capacity is 0.75 bits/s/Hz, compared with 1.5 bits/s/Hz in the narrowband case. Wideband capacity results

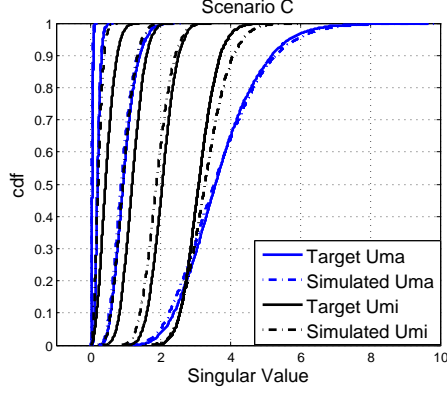


Figure 7. CDFs of the singular values for scenario C

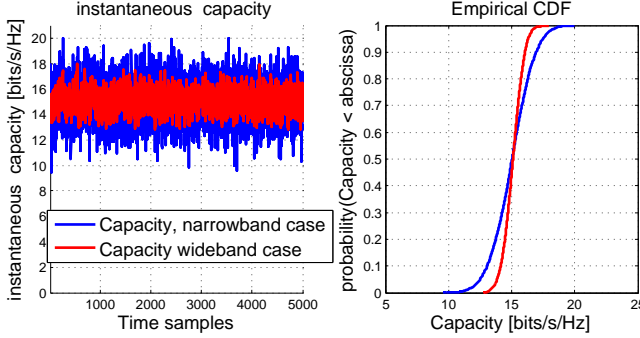


Figure 8. The instantaneous capacity in narrowband and wideband case for the FaKH14simulated SCME Umi TDL channel models for scenario C (left) and their cumulative distribution function (CDF) plots. The SNR  $\sigma$  is 15dB.

are shown in the following simulations unless otherwise stated.

3) *Capacity Simulation results:* CDF plots of the capacity for scenario A, B and C are shown in Figure 9, 10 and 11, respectively.

In scenario A, although the spatial correlation results at the Rx side for the Umi model and for the Uma models are different (as shown in Figure 3 and Figure 4), the capacity difference is negligible, as shown in Figure 9. This is due to the fact the Tx antennas are fully correlated for both channel models and spatial multiplexing is not supported. Therefore the capacity results are equally low for both channel models. As shown in Figure 10, in scenario B, the capacity for the Umi model is higher than the capacity for the Uma model. The capacity gain for the Umi channel model, compared to scenario A, is a result of low spatial correlation both at the Tx and at the Rx side. However, for the Uma channel model, the capacity gain compared with scenario A is negligible, as the spatial correlation at the Tx side and the Rx side are still high, with  $\rho^{Tx} = 0.9$  and  $\rho^{Rx} = 0.6$ . As shown in Figure 11, in scenario C, the capacity for the Umi model is higher than for the Uma model, as the spatial correlation correlation at the Tx side for the Uma model is always above 0.6, where the Tx side correlation is 0 for the Umi model, as shown in Figure 5.

The simulated capacity results match very well with the target capacity results for both channel models in scenario A and scenario B. The maximum antenna spacing at the Rx is  $0.5\lambda$  for scenario A and B. As shown in Figure 3 and Figure 4, the Rx side channel spatial characteristics can be accurately modeled in a test area of  $0.7\lambda$  with eight OTA probes.

The simulated capacity results are smaller than the target capacity results for scenario C for both channel models, with a mean difference of around 0.2 bits/s/Hz for the Uma model and 1.6 bits/s/Hz for the Umi model. The small deviation for the Uma channel model is due to the fact that the simulated and target spatial correlation at the Tx side are high (i.e. Tx correlation between any two elements larger than 0.65), which will cause a dramatic capacity reduction with  $C$  and  $\hat{C}$  being equally low. The median capacity is 10.6 bits/s/Hz for the Uma model, compared with 16.3 bits/s/Hz for the Umi model. For the Umi channel model, the capacity difference is substantial. As the spatial correlation at the Tx side is low (close to 0), the difference is caused by deviation between the target and simulated channels at the Rx side. The maximum antenna spacing at the Rx is  $1.5\lambda$  in scenario C, while the Rx side channel spatial correlation can only be modeled accurately when the antenna separation is smaller than about  $0.7\lambda$ , as shown in Figure 3. For the SCME Umi channels, the simulated spatial correlation at the Rx side  $\hat{\rho}_{13}^{Rx}$  (with antenna spacing  $1.0\lambda$ ) and  $\hat{\rho}_{14}^{Rx}$  (with antenna spacing  $1.5\lambda$ ) are 0.4 and 0.8 respectively, compared with both  $\rho_{13}^{Rx}$  and  $\rho_{14}^{Rx}$  less than 0.1 for the target curve, as shown in Figure 3. Therefore, we see a difference between the capacity of the simulated channel  $\hat{C}$  and the capacity of the target channel  $C$ .

In summary, if the Tx correlation is high, the channel simulation accuracy at the Rx side is irrelevant to the capacity, as the channel is ill-conditioned and the capacity results will be equally low for the simulated and target channel model. Nevertheless, the number of probes may affect the Rx power level in simulation with practical DUT antennas, and thus the throughput results might be affected by the number of probes in the measurements. This impact is not present in the capacity simulation results in this paper, as channel normalization and omnidirectional DUT antennas at the Rx are assumed. However, for practical OTA measurements (e.g. throughput measurement), absolute power without normalization is used. When the spatial correlation at the Tx side is low, the capacity of the simulated channels will follow that of the target channels within the test area where  $|\rho^{Rx} - \hat{\rho}^{Rx}|$  is small. When the DUT is outside the test zone area, we might see a difference between  $C$  and  $\hat{C}$ , as explained in Section III-D. Note that in reality, a Tx correlation  $\rho^{Tx}$  close to 1 is not very likely with practical antennas for realistic channels. It is selected in the paper for some scenarios to emphasize the importance of Tx correlation impact in channel simulation, which has not been considered in the literature.

#### D. Test zone size analysis

As explained earlier, it is desirable that the test zone size is defined using data rate deviation of the simulated channel in the laboratory compared to the target channel model. Data



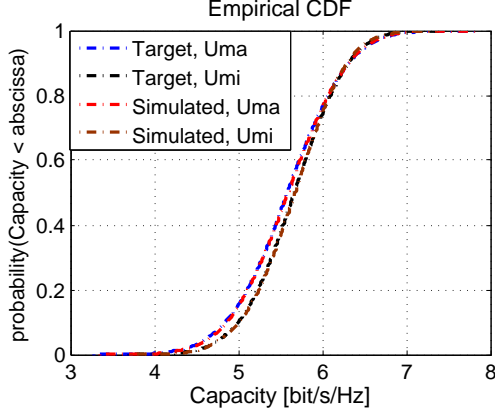


Figure 9. CDF plots of the capacity results for scenario A with average SNR  $\sigma = 15$  dB.

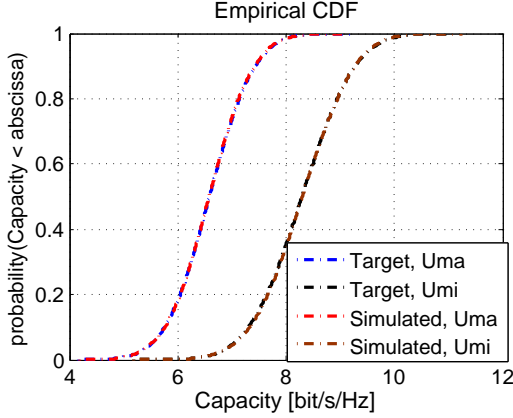


Figure 10. CDF plots of the capacity results for scenario B with average SNR  $\sigma = 15$  dB.

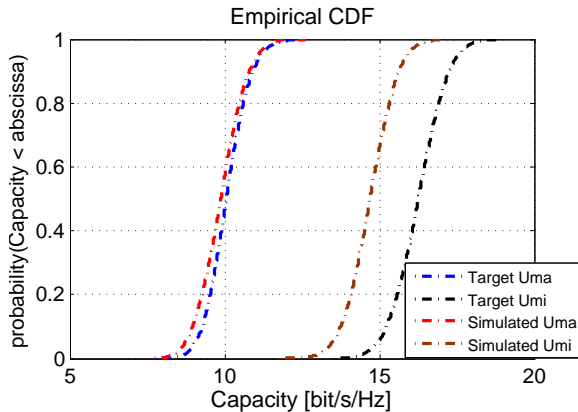


Figure 11. CDF plots of the capacity results for scenario C with average SNR  $\sigma = 15$  dB.

rate is one of the main factors that has direct influence on end-user experience. Data rate (i.e. throughput) is used as the metric for the characterization of active MIMO terminals in MIMO OTA standardization. Although data rate deviation under the target and simulated channels depend on how well the correlation is reproduced, it is desirable that the test zone size is defined using data rate deviation directly. Channel capacity is the theoretical upper bound on the data rate that can be reliably transmitted over a communications channel. We can express the test zone size in terms of how accurately the capacity of the simulated channel model  $\hat{C}$  matches the target channel model  $C$ . As shown earlier, the Rx side spatial characteristics simulation accuracy become irrelevant when correlation at the Tx side is high. To ensure that the capacity results are sensitive to spatial characteristics at the Rx side in the example, the spatial correlation at the Tx side is selected to be low. In the following, the settings of scenario C for the Tx antenna array and the Umi channel model are selected. At the Rx side, the ULA antenna element spacing ranges from  $0.1\lambda$  to  $0.5\lambda$  in steps of  $0.1\lambda$ , which corresponds to maximum antenna separation ranging from  $0.3\lambda$  to  $1.5\lambda$  with  $0.3\lambda$  step for a 4 element ULA. The CDF plots of the capacity results for various antenna spacings for the Umi channel model are shown in Figure 12. The mean capacity of the target and simulated channel models for the  $4 \times 4$  MIMO system with different maximum antenna separations among elements in the Rx are shown in Table III. As can be seen, the capacity deviation  $|C - \hat{C}|$  is up to  $0.2$  bits/s/Hz when the maximal antenna separation is smaller than  $0.9\lambda$  (i.e. antenna spacing less than  $0.3\lambda$ ). Although  $|\rho^{Rx} - \hat{\rho}^{Rx}|$  is around  $0.25$  at  $0.9\lambda$  maximum antenna separation, as shown in Figure 3, the capacity deviation  $|C - \hat{C}|$  is only  $0.2$  bits/s/Hz. This is due to the fact that  $|\rho - \hat{\rho}|$  is less critical with small  $|\rho|$  ( $|\rho| = 0.3$ ). At maximal antenna separation  $1.2\lambda$  (i.e antenna spacing  $0.4\lambda$ ), the capacity deviation  $|C - \hat{C}|$  is  $0.9$  bits/s/Hz, as  $\rho^{Rx}$  is close to  $0$ , compared with  $\hat{\rho}^{Rx}$  in the high correlation region ( $\hat{\rho}^{Rx} = 0.8$ ). As shown in the simulation results, the test area size is limited, regardless of the metric used. With an eight-probe setup, the test area size is limited to  $0.7\lambda$  with threshold  $|\rho^{Rx} - \hat{\rho}^{Rx}| \leq 0.1$ , compared with the test area size limited to  $0.9\lambda$  with threshold  $|C - \hat{C}| \leq 0.2$  bits/s/Hz.

As can be seen from the simulation results, the capacity simulation accuracy depends highly on the Tx correlation, the Rx correlation and the Rx correlation simulation accuracy. The capacity error represents the simulated data rate deviation from the target expected data rate, while it obscures the information on the physical characteristics of the simulated channel. For example, it might be difficult to explain the system performance under certain channel models and the Tx/Rx configurations without knowing the correlation level at the Tx and Rx side. Note that the test area size in terms of capacity simulation accuracy or correlation simulation accuracy at the Rx side is determined by the predefined corresponding error thresholds. In the literature, a maximum correlation error of  $0.1$  or rms correlation error of  $0.05$  are often assumed. However, it is not clear whether such error thresholds in correlation error would result in a difference in MIMO device performance, e.g. the throughput. The focus of the study is to propose a metric to

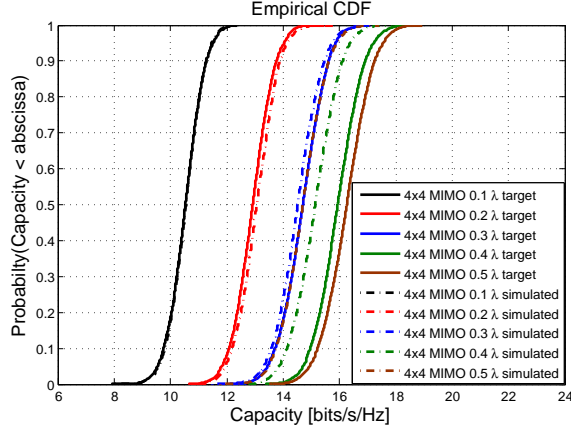


Figure 12. CDF plots of the capacity for scenario C with different antenna spacing for the Rx ULA with average SNR  $\sigma = 15$  dB. The antenna element spacing in the ULA is shown in the legend for each curve.

Table III  
MEAN CAPACITY FOR THE  $4 \times 4$  MIMO SYSTEM WITH DIFFERENT ANTENNA SPACING [CAPACITY UNIT: BITS/S/Hz].

Antenna element spacing	$0.1\lambda$	$0.2\lambda$	$0.3\lambda$	$0.4\lambda$	$0.5\lambda$
$\bar{C}$	10.5	12.9	14.7	16.0	16.3
$\hat{\bar{C}}$	10.5	13.1	14.5	15.1	14.7
$ \bar{C} - \hat{\bar{C}} $	0	0.2	0.2	0.9	1.6
$ \rho_{14} $	0.59	0.06	0.04	0.09	0.02
$ \rho_{14} - \hat{\rho}_{14} $	0	0.01	0.25	0.69	0.83

determine the error level for a specific multi-probe anechoic chamber system and considered target propagation channel within the test area. If the error thresholds for the capacity simulation error are defined by the standard bodies or other groups, the acceptable test area size with a limited number of probes can be calculated. As shown in Table III, relative capacity errors for  $0.3\lambda$  and  $0.4\lambda$  antenna element spacing (i.e.  $0.9\lambda$  and  $1.2\lambda$  maximum antenna separation) are 1.4% and 5.6% respectively. However, correlation errors are 0.25 and 0.69 for  $0.9\lambda$  and  $1.2\lambda$  maximum antenna separation cases, respectively, indicating a high sensitivity of correlation error as a metric. For the same relative threshold, relative capacity error could result in a larger test size area.

#### IV. MEASUREMENT VERIFICATION

A measurement campaign was carried out in a practical setup at Anite Telecoms Oy, Finland to verify the capacity analysis results presented in Section III. Figure 1 illustrates the test setup. Figure 13 shows parts of the practical probe configuration in the anechoic chamber. Eight uniformly located probes on the azimuth ring were connected to an Anite Prosim F32 to synthesize the channel (with only 8 channel emulator output ports connected), while the rest of the probes on the other rings were not connected. A sledge and turntable that support radial and rotational movement, respectively, of the calibration dipole were used in the measurements.

Phase and amplitude calibrations are performed for each probe before the measurements, although the phase calibration

is not required with the PFS technique, as explained in [3]. The basic idea is to record the channel matrices using the calibration dipole in several positions and calculate the capacity based on Eq. (5). The measurement procedure is similar to the spatial correlation measurements detailed in [2]. Summarizing, for CIRs that are associated with each Tx antenna, the channel emulator is paused every 10 CIRs (with 4 CIRs per wavelength) to satisfy the Nyquist criteria and  $S_{21}$  is measured with the network analyzer and saved for post-processing. 2000 CIRs were recorded in the measurements. The sweep of the same CIRs is repeated for all the seven test positions, as shown in Figure 1. Then the same procedure is repeated for the CIRs associated with other Tx antennas in a sequential manner.

Note that the simulated channels in the multi-probe setup, as shown in Figure 2, have multiple different delays. The geometry based stochastic channels are generally frequency selective channels, and the DUT will be evaluated under the generated wideband channel models. Narrowband measurements were performed to save measurement time. As shown in the simulation results in Section III-C2, the difference between wideband and narrowband mean capacity is negligible. The frequency responses were recorded at frequency  $f = 2.14$  GHz. One important aspect related to practical measurements is that we should ensure that the absolute power levels associated with different Tx antennas in the calibration are the same (or at least known).

As the measurement was conducted in an anechoic chamber, the noise and interference inside the measurement can be considered insignificant. Note that neither interference nor noise were emulated with the channel emulator in the measurements. Only the frequency responses of the channel at a single frequency were recorded. The capacity of the measured channels is calculated assuming an average SNR  $\sigma = 15$  dB. Other SNR values can be used in the calculation as well. Note that it is a mandatory step to analyze the sources of errors and uncertainties in the measurements. Some investigations on measurement uncertainty were reported, see e.g. in [22], where some error sources were identified and analyzed. Testing items, e.g. turntable stability, signal drifting level in the channel emulator and power amplifiers, power coupling level among probes, reflection level inside the anechoic chamber and cable effects were investigated. Phase and amplitude drifting of the whole OTA system were up to  $6^\circ$  and 0.3 dB over 6 hours. Co-polarized probe coupling was below -30dB and cross-polarized probe coupling was below -20dB. It was found that a choke/cartridge or Ferrite-loaded cable can help minimize the cable effects. The uncertainty level, after careful system calibration is quite small in the measurements, as demonstrated by the measured field synthesized results in [22]. Quantifying the uncertainty levels in practical multi-probe anechoic chamber setups and their impact on performance parameters, e.g. signal correlation accuracy, capacity and throughput is beyond the scope of the paper.

In the measurements, the settings of scenario B for the Tx antenna array presented in Section III was selected, and both the Uma and Umi channel models are investigated. To understand capacity simulation accuracy as a function of

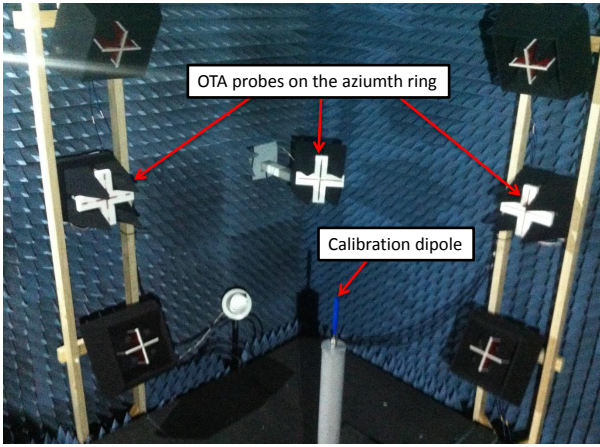


Figure 13. Illustration of part of the practical probe setup in the anechoic chamber. The measurement was done at  $f = 2.14$  GHz

antenna separation at the Rx side for both channel models, virtual arrays consisting of two antenna elements with different antenna spacings were used for the Rx, as shown in Figure 1. A single dipole at seven positions were used to record CIRs in the measurement and to form virtual arrays at the Rx side. Note that the same channel models were reproduced in the multi-probe setup for each measurement position. The spacing increment between antenna elements was  $0.2\lambda$ , as opposed to  $0.1\lambda$  in previous sections, to save measurement time. Hence, six  $2 \times 2$  MIMO matrices with different antenna separations at the Rx side could be formed.

Mean capacity  $C$  results for the target channel model, mean capacity  $\hat{C}$  for the simulated channel and mean capacity  $C_m$  for the measured channel for both the Umi and Uma channel models are shown in Figure 14. The spatial correlation at the Rx side and at the Tx side for the two channel models are shown in Figure 3, Figure 4 and Figure 5, respectively. The measured spatial correlation matches very well with the simulated correlations at the Tx and Rx for both the Umi and Uma channel models, with a deviation between the measured and simulated correlation up to 0.03.

The capacity for the Uma model is generally lower than for the Umi channel. The deviation  $|C - \hat{C}|$  is generally small for the Uma channel model, as the correlation at the Tx side is high. For the Umi channel model,  $|C - \hat{C}|$  is rather small when antenna separation is smaller than  $1\lambda$ . Similar observations have been made and explained for scenario B in section III-C3. As shown in Figure 14, the measured mean capacities  $C_m$  matches well with the simulated mean capacities  $\hat{C}$  for both the Uma and Umi channel models, with a deviation up to 0.2 bits/s/Hz.

## V. CONCLUSION

One of the key questions to be addressed in the multi-probe anechoic MIMO OTA testing is how large a test area can be supported with a limited number of probes. The current work investigates wideband MIMO channel capacity in multi-probe anechoic chamber setups, with an emphasis on the relationship between capacity simulation accuracy and test area size. The investigation is based on the well accepted channel models in

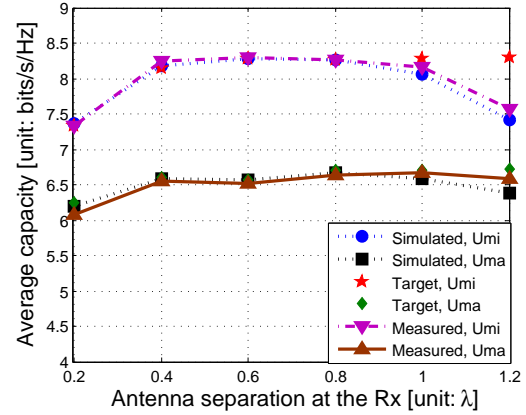


Figure 14. Mean capacity of the target channel model ( $C$ ), mean capacity of the simulated channel ( $\hat{C}$ ) and mean capacity of the measured channel ( $C_m$ ) for the SCME Umi and SCME Uma TDL channel models.

the 3GPP LTE standards for over the air testing of MIMO capable terminals, i.e. the SCME Umi TDL and SCME Uma TDL models. For these models, the simulation results show that it is irrelevant how well the spatial characteristics at the Rx side are reproduced when the spatial correlation at the Tx side is in the high region (e.g.  $\rho > 0.7$ ), as both the simulated capacity and target capacity will be equally low. With a limited number of probes in the multi-probe setup, the test area size is generally limited when the spatial correlation at the Tx side is in the low region, regardless of the metric used to determine the test area size. Both spatial correlation based and capacity based metrics have demonstrated this effect. However, the capacity simulation accuracy is less sensitive to spatial correlation simulation error at the Rx with a small target correlation at the Rx side. Simulation results have shown that the capacity deviation  $|C - \hat{C}|$  is less than 0.3 bits/s/Hz up to  $1\lambda$  wavelength for the Umi channel models, as  $|\rho^{Rx} - \hat{\rho}^{Rx}|$  is less critical when  $|\rho^{Rx}|$  is small ( $|\rho^{Rx}| = 0.3$ ). The simulation results are further supported by measurements in a practical multi-probe anechoic chamber setup.

## ACKNOWLEDGMENT

The authors appreciate the help and discussions from colleagues in Anite Telecoms Oy, especially Mr. Lassi Hentilä and Mr. Jouni Uusimaa with the practical measurements.

## REFERENCES

- [1] A. Paulraj, D. Gore, R. Nabar, and H. Bolcskei, "An overview of MIMO communications - a key to gigabit wireless," *Proceedings of the IEEE*, vol. 92, no. 2, pp. 198–218, Feb 2004.
- [2] "Verification of radiated multi-antenna reception performance of User Equipment," 3GPP, TR 37.977 V1.0.0, Sep. 2013.
- [3] P. Kyösti, T. Jämsä, and J. Nuutinen, "Channel modelling for multiprobe over-the-air MIMO testing," *International Journal of Antennas and Propagation*, 2012.
- [4] A. Khatun, H. Laitinen, V.-M. Kolmonen, and P. Vainikainen, "Dependence of Error Level on the Number of Probes in Over-the-Air Multiprobe Test Systems," *International Journal of Antennas and Propagation*, vol. 2012, 2012.

- [5] W. Fan, X. Carreño, J. Ø. Nielsen, M. B. Knudsen, and G. F. Pedersen, "Channel Verification Results for the SCME models in a Multi-Probe Based MIMO OTA Setup," in *Vehicular Technology Conference (VTC Fall)*. IEEE, September 2013, pp. 1–5.
- [6] A. Scannavini, F. Chauvet, and N. Gross, "MIMO OTA measurement with anechoic chamber method," in *Antennas and Propagation (EuCAP), 2013 7th European Conference on*. IEEE, April 2013.
- [7] W. Fan, F. Sun, P. Kyösti, J. Nielsen, X. Carreño, M. Knudsen, and G. Pedersen, "3D channel emulation in the multi-probe setup," *Electronics Letters*, vol. 49, pp. 623–625(2), April 2013.
- [8] M. Chiani, M. Z. Win, and A. Zanella, "On the capacity of spatially correlated MIMO Rayleigh-fading channels," *Information Theory, IEEE Transactions on*, vol. 49, no. 10, pp. 2363–2371, 2003.
- [9] V. Jungnickel, S. Jaeckel, L. Thiele, L. Jiang, U. Kruger, A. Brylka, and C. Von Helmolt, "Capacity measurements in a cooperative MIMO network," *Vehicular Technology, IEEE Transactions on*, vol. 58, no. 5, pp. 2392–2405, 2009.
- [10] D. shan Shiu, G. Foschini, M. Gans, and J. Kahn, "Fading correlation and its effect on the capacity of multielement antenna systems," *Communications, IEEE Transactions on*, vol. 48, no. 3, pp. 502–513, Mar 2000.
- [11] 3GPP, "Tp for tr 37.977 to address high correlation behaviour in the uma model," *3GPP R4-130901*, Sep. 2013.
- [12] D. Baum, J. Hansen, and J. Salo, "An interim channel model for beyond-3G systems: extending the 3GPP spatial channel model (SCM)," in *Vehicular Technology Conference, 2005. IEEE 61st*, vol. 5, 2005, pp. 3132–3136 Vol. 5.
- [13] "Spatial channel model for Multiple Input Multiple Output (MIMO) simulations (Release 11)," 3GPP/3GPP2, TR 25.996 V11.0.0, Sep. 2012.
- [14] L. Hentilä, P. Kyösti, M. Käske, M. Narandzic, and M. Alatossava, "MATLAB implementation of the WINNER Phase II Channel Model ver1. 1," 2007.
- [15] W. Fan, J. Nielsen, O. Franek, X. Carreno, J. Ashta, M. Knudsen, and G. Pedersen, "Antenna pattern impact on mimo ota testing," *Antennas and Propagation, IEEE Transactions on*, vol. 61, no. 11, pp. 5714–5723, Nov 2013.
- [16] W. Fan, X. de Lisbona, F. Sun, J. Nielsen, M. Knudsen, and G. Pedersen, "Emulating Spatial Characteristics of MIMO Channels for OTA Testing," *Antennas and Propagation, IEEE Transactions on*, vol. 61, no. 8, pp. 4306–4314, 2013.
- [17] N. Czink, "The random-cluster model: a stochastic mimo channel model for broadband wireless communication systems of the 3rd generation and beyond," *Available at: publik.tuwien.ac.at/files/PubDat\_112121.pdf*, 2007.
- [18] R. Vaughan and J. B. Andersen, "Channels, propagation and antennas for mobile communications." Institution of Electrical Engineers, 2003.
- [19] C. Oestges, "Validity of the Kronecker Model for MIMO Correlated Channels," in *Vehicular Technology Conference, 2006. VTC 2006-Spring. IEEE 63rd*, vol. 6, May 2006, pp. 2818–2822.
- [20] "Spatial channel model for multiple input multiple output (MIMO) simulations," 3GPP/3GPP2, TR 25.996 V6.1.0, 2003.
- [21] J. Nielsen, B. Yanakiev, S. Barrio, and G. Pedersen, "Channel statistics for mimo handsets in data mode," in *Antennas and Propagation (EuCAP), 2014 8th European Conference on*, 2014.
- [22] W. Fan, I. Szini, M. Foegelle, J. Nielsen, and G. Pedersen, "Measurement uncertainty investigation in the multi-probe ota setups," in *Antennas and Propagation (EuCAP), 2014 8th European Conference on*, April 2014, pp. 1068–1072.